

PCCP

Accepted Manuscript



This is an *Accepted Manuscript*, which has been through the Royal Society of Chemistry peer review process and has been accepted for publication.

Accepted Manuscripts are published online shortly after acceptance, before technical editing, formatting and proof reading. Using this free service, authors can make their results available to the community, in citable form, before we publish the edited article. We will replace this *Accepted Manuscript* with the edited and formatted *Advance Article* as soon as it is available.

You can find more information about *Accepted Manuscripts* in the [Information for Authors](#).

Please note that technical editing may introduce minor changes to the text and/or graphics, which may alter content. The journal's standard [Terms & Conditions](#) and the [Ethical guidelines](#) still apply. In no event shall the Royal Society of Chemistry be held responsible for any errors or omissions in this *Accepted Manuscript* or any consequences arising from the use of any information it contains.

Structural evolution of Ag-Cu nano-alloys confined between AlN nano-layers upon fast heating

J. Janczak-Rusch, M. Chiodi, C. Cancellieri, F. Moszner, R. Hauert, G. Pigozzi,
L.P.H. Jeurgens

Abstract

The structural evolution of Ag-Cu/AlN nano-multilayer (NML), as prepared by a magnetron-sputtering on a α -Al₂O₃ substrate, was monitored during fast heating by real-time in-situ XRD analysis (at the synchrotron), as well as by ex-situ microstructural analysis using SEM, XPS and in-house XRD. The as-deposited NML is constituted of alternating nano-layers (thickness \approx 10 nm) of a chemically inert AlN barrier and a eutectic Ag-Cu_{40at.%} nano-alloy. The nano-alloy in the as-deposited state is composed of a fcc matrix of Ag nano-grains (\approx 6 nm), which are supersaturated by Cu, and some smaller embedded Cu rich nano-grains (\approx 4 nm). Heating up to 265°C activates segregation of Cu out of the supersaturated Ag nano-grains phase, thus initiating phase separation. At $T > 265$ °C, phase-separated Cu metal partially migrates to the top NML surface, thereby relaxing thermally-accumulated compressive stresses in the confined alloy nano-layers and facilitating grain coarsening of (still confined) phase-separated nano-crystallites. Further heating and annealing up to 420°C results in complete phase separation, forming extended Ag and Cu domains with well-defined coherent Ag/AlN interfaces. The observed outflow of Cu well below the eutectic melting point of the bulk Ag-Cu alloy might provide new pathways for designing low-temperature nano-structured brazing materials.

Keywords: Ag-Cu eutectic; size effect; brazing filler; melting point depression; nano-joining.

1. Introduction

The Ag-Cu system is of broad-interest from both a scientific and technological point of view. On the one hand, the Ag-Cu system serves as a model system to investigate the phase stability of metastable solid solutions, as prepared by various non-equilibrium processing routes (e.g. vapour and splat quenching, mechanical alloying, vapour deposition, ion beam mixing).¹⁻⁶ On the other hand, Ag-Cu-based alloys are among the most commonly used braze alloys for joining a wide variety of material combinations.⁷⁻¹¹

The eutectic Ag-Cu alloy has an composition of Ag-40 at.% Cu and a melting point of 779 °C, much below the bulk melting temperatures of constituting pure fcc metals Ag and Cu of 962 °C and 1083 °C, respectively. The large atomic size mismatch (13%) between Ag and Cu results in a large positive heat of mixing in both the solid and liquid state. Consequently, Ag and Cu are practically immiscible below ~300 °C (the mutual solubility of Cu and Ag in equilibrium is less than 1 at.% at room temperature) and, consequently, a large driving force for phase segregation of quenched (i.e. meta-stable) Ag-Cu solid solution phases exists below the eutectic melting temperature.⁶

Production of Ag-Cu alloys by non-equilibrium processing routes typically results in a complex metastable phase constitution: a supersaturated crystalline (fcc) Ag-Cu solid solution^{2,6}, a mixture of (supersaturated) α -Ag and β -Ag nano-crystallites (i.e. Ag and Cu fcc nano-crystals with substitutionally dissolved Cu and Ag, respectively)¹¹, a hexagonal (4H) phase¹³ and/or (occasionally) an amorphous solid solution¹⁻². Substantial mutual solubility of Ag and Cu (up to 10 at.%) has been found for vapour-deposited¹⁴ and sputtered Ag-Cu thin films¹⁵; the solubility (and degree of supersaturation) increases with decreasing substrate temperature during deposition (increasing quenching rate)⁶. The average nano-crystallite size in such Ag-Cu films is in the range of 1.6 – 5 nm (as determined by XRD and/or TEM).^{13,16-18} As emphasized in Ref.¹⁷, reported claims of *homogeneous* Ag-Cu solid solutions have likely undergone (incipient or partial) phase separation on ultrafine scales that escaped detection (*note*: composition modulations on the scale of 1 nm are difficult to image, even by advanced TEM methods).

To rationalize phase stabilities in low-dimensional systems, such as in Ag-Cu nanoparticles and Ag-Cu thin films, it is important to recognize that the surface energy of Ag (1.25 J/m²) is considerably lower than that of Cu (1.79 J/m²)¹⁹, which provides a strong driving force for Ag to segregate at the free surface²⁰. Moreover the melting point of nanoparticles and thin-films is known to decrease with size at the nano-scale, as governed by the

increased surface-to-volume ratio.^{21,22} Several theoretical predictions and experimental verifications of e.g. surface segregation, size-dependent melting (i.e. a melting point depression) and the size- and shape-dependence of the eutectic composition and melting temperature have been reported for Ag-Cu nano-particles and Ag-Cu thin films.^{20,22,24-26} These previous studies have shown that, in parallel with a size-dependent decrease of the eutectic melting temperature, the eutectic composition of Ag-Cu nano-particles and Ag-Cu thin films shifts to the Ag-rich side of the respective Ag-Cu bulk phase diagram. For example, for 10 nm thick Ag-Cu films levitating in vacuum, the eutectic composition and melting point is predicted to shift to about 76 at.% Ag and 726°C, respectively (*note*: the corresponding shifts are somewhat higher for Ag-Cu nano-particles with a corresponding diameter of 10 nm).²³

Evidently the phase stability of a nano-alloy in (partial) contact with vacuum (e.g. nano-particles and thin films) may principally differ from that of the same nano-alloy embedded in a solid matrix (e.g. nano-composites, nano-multilayer). Namely the melting behaviour of metallic nanoparticles, as confined in a chemically-inert solid matrix with a much higher melting point (e.g. typically an oxide, nitride or refractory metal), will not only depend on particle size, but predominantly also on the (defect) structure of the particle-matrix interface and the thermal stresses evolving upon heating (due to the thermal expansion differences between the particle and the matrix).²⁷ As a rule of thumb, an incoherent interface between the nano-particle and an inert matrix phase favours interfacial pre-melting (resulting in a melting point depression; MPD), whereas the corresponding coherent particle-matrix interface obstructs interfacial pre-melting (causing superheating).²⁸⁻³⁰ To the best of our knowledge, the phase stability of confined eutectic Ag-Cu nano-alloys embedded in an inert matrix phase has not been addressed up to date.

Recently Ag-Cu nano-paste has been proposed for high-temperature die-attach applications.³¹ However, such nano-particle-based joining technologies have to deal with complex handling and safety issues. To bypass these critical issues, our research aims at the development of nano-structured Ag-Cu braze fillers with a reduced melting point as compared to conventionally applied braze alloys, which can be produced as a coating or as a foil by conventional thin-film deposition techniques.³² The current paper presents a first comprehensive experimental investigation of the structural evolution of eutectic Ag-Cu nano-alloys, as confined between inert AlN barriers in a nano-multilayered configuration, upon fast heating. To this end, Ag-Cu/AlN nano-multilayers (NMLs) were deposited on sapphire substrates by magnetron sputtering. The produced Ag-Cu/AlN NMLs are constituted of

alternating nano-layers of Ag-Cu braze alloy with a bulk-eutectic composition (i.e. 40at.% Cu) and a thin AlN barrier, which serves as a chemically inert barrier to confine the alloy to the nano-scale up to its melting point. AlN was selected as a barrier, because it has a considerably higher melting point (2200 °C) than Ag metal, Cu metal and the eutectic Ag-Cu alloy. Moreover AlN is chemically inert to Ag and Cu within the investigated temperature range (up to 420 °C).

The microstructural evolution of the Ag-Cu/AlN NMLs was monitored in real-time during fast heating from room temperature (RT) up to 420 °C by in-situ X-ray diffraction at the synchrotron. Furthermore the microstructure (e.g. layer thicknesses, morphology, phase constitution, texture) of the as-deposited and heat-treated NMLs was characterized ex-situ by a combinatorial analytical approach, applying scanning electron microscopy (SEM), X-ray photoelectron spectroscopy (XPS) and X-ray diffraction (XRD) analysis. The thus obtained results are discussed in terms of the structural evolution of confined eutectic Ag-Cu nano-layers upon heating up to 420 °C.

2. Experimental

2.1 Materials and experimental setup

Ag-Cu_{40at.%}/AlN nano-multilayers (NMLs) were deposited on 2" epi-polished α -Al₂O₃(1 $\bar{1}$ 02) single-crystalline wafer substrates (i.e. sapphire-R wafers) by magnetron sputtering in a high vacuum chamber (base pressure < 1×10⁻⁸ mbar) from two confocally arranged unbalanced magnetrons equipped with 2" targets of pure Al (99.99% purity, as supplied by Kurt J. Lesker, USA) and of an eutectic Ag-Cu_{40at.%} alloy. The eutectic Ag-Cu_{40at.%} alloy target was produced by melting a commercial Cusil filler metal foil (Wesgo Metals, USA) of the same composition in an alumina crucible under a protective Ar (93 vol.%) – H₂ (7 vol.%) gas atmosphere and subsequently shape-casting into the desired form. Note that the α -Al₂O₃(1 $\bar{1}$ 02) substrate is chemically inert with respect to the deposited Ag-Cu/AlN NML system (at least up to 420 °C) and its main diffraction reflections (10 $\bar{2}$) and (20 $\bar{4}$) do not overlap with the ones originating from metallic Ag and Cu.

The α -Al₂O₃(1 $\bar{1}$ 02) substrates were ultrasonically cleaned in acetone and isopropanol before introduction into the sputter chamber. Before each deposition run, possible surface contamination on the α -Al₂O₃(1 $\bar{1}$ 02) substrate (mostly adventitious C) was removed by Ar⁺ sputter cleaning for 5 min applying a RF Bias of 100V. Next, Ag-Cu/AlN NMLs were produced by consecutive deposition of a 10 nm-thick AlN buffer layer and 21 alternations of a

10 nm-thick (Ag-Cu_{40at.%}) layer and a 10 nm thick AlN barrier layer. Here it is noted that the aforementioned layer thicknesses denote nominal thicknesses as estimated from the calibrated sputter rates of Ag, Cu and AlN (see Sec. 3 for respective layer thickness values from cross-sectional SEM analysis). The AlN deposition steps were performed by DC reactive sputtering from the Al target in a Ar/N₂ reactive mixture (2:1 ratio) applying a target power of 200 W. The sputtering parameters were adjusted to obtain a deposition rate of about 5 nm/min. The Ag-Cu layers deposition was performed from an Ag-Cu_{40at.%} target in a pure Ar atmosphere at 25 W target power (corresponding to a deposition rate of about 5.5 nm/min). During the deposition, the substrate was rotated at a constant speed of 40 rpm. The sputtering process did not involve any active substrate cooling, thus the specimen temperature gradually increased from room temperature to about 40 °C after 1 h of deposition.

The microstructural evolution of the NMLs was in-situ monitored from room-temperature (RT) to 420 °C by real-time synchrotron XRD at the Swiss Light Source, Material Science beamline (for instrumental details, see Sec. 2.2). The beamline setup was equipped with a custom-designed furnace for in-situ heating (HTK 16 MSW), as operated under shielding gas (i.e. the chamber was continuously flooded with Ar at slight atmospheric overpressure). Such furnace was especially designed and modified to allow transmission diffraction experiments. The applied temperature ramp during in-situ heating and simultaneous XRD analysis is shown in Fig. 1. First, the specimen was pre-heated up to 250 °C and thermally equilibrated for roughly 15 min. Next, the specimen was heated up to 320 °C at an nearly constant rate of 4.6 K/min and subsequently up to 420 °C at maximum power (of the ceramic heating plate) resulting in a heating rate of 20 K/min. The specimen was kept at 420 °C for 40 min, after which the heat source was switched off, allowing the sample to freely cool down to room temperature.

2.2 Analysis and data evaluation

The phase constitution, texture, morphology and defect structure of the as-deposited and thermally-treated NML were studied by SEM, XRD and XPS. Cross-sections for the SEM investigations were prepared by a Hitachi IM4000 Ar ion milling system applying an acceleration voltage of 6 kV and a swing angle of $\pm 30^\circ$. High resolution imaging of the as-deposited and thermally-treated NMLs was performed with a Hitachi S-4800 SEM (operating at 5kV). Combined SEM and energy dispersive X-ray (EDX) analysis was conducted using a Hitachi S-3700 (operating a 20kV) equipped with an EDAX Octane Pro detector. Ex-situ XRD analysis of the as-deposited and thermally-treated NMLs was performed using a Bruker

Discover (D8) X-Ray Diffractometer, operated in either Bragg-Brentano mode (for collecting theta-2theta (2θ) scans and rocking curves (RC)) or in grazing-incidence geometry (for collecting 2theta (2θ) scans, while fixing the incident angle at 5° to enhance the signal contribution from the top layers of the NML). In addition, in-plane texture measurements (i.e. pole figures) of the principle Ag, Cu and AlN reflections were recorded before and after heating.

The thermal evolution of the system was monitored in-situ using real-time XRD in transmission mode at the Swiss Light Source, Material Science (X03MA) beamline. Such beamline is conceived to provide X-Rays in the energy of 5-40 keV for powder diffraction and surface diffraction experiments. A photon energy of 20 keV was chosen ($\lambda = 0.61986 \text{ \AA}$) and our experiments were carried out on the powder diffraction branch using a MYTHEN single-photon-counting silicon micro-strip detector, which allowed acquisition of the diffraction patterns over 120° in 2θ in less than 40 s. Hence at least one 2θ spectrum (with a good S/N ratio) could be recorded every 10° C during fast heating at a rate up to 20 K/min (a detailed description of the beamline setup and the detector are given in Refs. ^{34,35}, respectively).

Ex-situ X-ray photoelectron spectra (XPS) analysis of the as-deposited and heat-treated NMLs was performed using Physical Electronics (PHI) Quantum 2000 instrument (base pressure of $< 4 \times 10^{-7} \text{ Pa}$), employing monochromatic incident Al $K\alpha$ radiation (1486.68 eV; spot size $100 \mu\text{m}$; electron take-off angle of 45°) and a hemispherical capacitor electron-energy analyser equipped with a channel plate and a position-sensitive detector. Composition–depth profiles were recorded by employing alternating cycles of XPS analysis and sputtering with a focused 1 kV Ar^+ beam rastering an area of $2 \times 2 \text{ mm}^2$. During each successive analysis step, detailed spectra of the O 1s, N 1s, Al 2s, Al 2p, C 1s, Ag $3d^{5/2}$ and Cu $2p^{3/2}$ core levels were recorded with a step size of 0.5 eV at a constant pass energy of 117.4 eV, which corresponds to an analyser energy resolution of 1.62 eV (as taken equal to the full-width-at-half-maximum of the Ag $3d^{5/2}$ peak). Compensation of surface charging during spectra acquisition was realized by simultaneous operation of an electron- and an argon ion-neutralizer during each analysis step. The estimated sputter rate was taken equal to 0.83 nm/min, as determined for a AlN thin-film reference with a known thickness of 30 nm.

The measured Cu 3s and Cu 3p core-level regions partially overlap with the Al 2s and Al 2p regions. Hence the Al 2s main peak had to be separated from the overlapping Cu 3s spectral contribution by linear-least squares fitting, using the Linear-Least Squares fitting routine in the Phi Multipack Software (version 8.2). Quantification of the resolved peak

intensities (areas) was performed by adopting the relative elemental sensitivity factors, as supplied by the manufacturer. Oxygen was only detected at the outer surface. To reduce the noise in the quantified O concentration-depth profile, the measured O 1s region was linear-least squares fitted with the dominant O signal recorded from the first cycle (corresponding to the unspattered outer surface).

Since Ag is preferentially sputtered from the Ag-Cu alloy³⁶, a steady-state enrichment of Cu will be established in the Ag-Cu alloy (sub)surface region upon sputtering. XPS measurements of a homogenous bulk eutectic Ag-Cu alloy reference after cumulative steps of sputtering-cleaning at 1 keV Ar⁺ indeed evidence a steady-state enrichment of 60 at.% Cu within 15 min of sputtering at 1 kV Ar⁺. To account for the preferential sputtering of Ag from the Ag-Cu alloy, quantification of the measured XPS depth profile of the as-prepared Ag-Cu/AlN NML was performed using the experimentally determined relative sensitive factors of Ag and Cu for the eutectic Ag-Cu alloy reference. As discussed in Sec. 3, the standard elemental sensitivity factors of Ag and Cu (as supplied by the manufacturer) were used for quantification of the sputter-depth profile of the phase-separated and Cu-depleted NML after heat treatment.

3. Results and discussion

3.1 As-deposited NML microstructure

A cross-sectional SEM image of the as-deposited NMLs is shown in Fig. 2a; the lighter and darker layers correspond to Ag-Cu and AlN, respectively. Since the SEM contrast for Al₂O₃ and AlN is very similar, the bottom (i.e. firstly deposited) AlN nano-layer on the α -Al₂O₃(1 $\bar{1}$ 02) substrate is not resolved. The cross-sectional SEM analysis evidences a highly regular periodicity of the alternating layers; each of the 21 repeating Ag-Cu/AlN stacking units is clearly resolved. The SEM analysis indicates that the nano-layers are laterally very uniform throughout the NML stack with an average layer thickness of \approx 15 nm for the Ag-Cu nano-alloy and \approx 11 nm for the AlN barrier. This complies well with the SEM analysis in planar view (insert in Fig. 2a), showing a very smooth surface for the as-deposited NML; i.e. no defects, such as cracks, hillocks or voids, were detected at the surface. Notably no phase contrast (due to e.g. phase separation) was observed by SEM within the Ag-Cu nano-layers in their as-deposited state (in contrast to the phase contrast visible after in-situ heat treatment; see Sec. 3.3).

The measured XPS composition-depth profile of the as-deposited NML confirms a nominal eutectic composition of 60 at.% Ag and 40 at.% Cu for the as-deposited Ag-Cu nano-layers, as well as a 1:1 stoichiometric composition of the as-deposited AlN layer (Fig. 2b). No O contamination was detected in the as-deposited Ag-Cu nano-layers (only at the outer NML surface some oxygen was detected).

X-ray diffractograms of the as-deposited Ag-Cu/AlN NMLs, as recorded at room temperature (RT) in transmission geometry at the synchrotron facility and in Bragg-Brentano geometry in the laboratory (see Sec. 2.2), are shown in Figs. 3a and 3b, respectively. Considering the differences in measurement geometry and beam intensity (much more intense at the synchrotron), the independent diffraction measurements are fully consistent. Both measurements evidence broad diffraction peaks from Ag, Cu and AlN and very narrow (and much more intense) reflections from the single-crystalline sapphire substrate. For the 2theta scans collected at the synchrotron (Fig. 3a), the Ag(222) line is superimposed on the narrow single crystal peak from the sapphire substrate and represents the strongest reflection from the NML structure. In addition, much weaker, broad reflections from Ag (i.e. Ag(311) and Ag(511)) and Cu (i.e. Cu(222)) are present. As discussed in the following, the large widths of the Ag, Cu and AlN peaks can be attributed to the combined effects of a nano-crystallite size, the presence of growth defects, internal stress/strain and nano-size confinement.³⁸

Fig. 3b evidences some modulations in the diffracted intensity in proximity of the Ag(111) peak. However, the diffractograms do not exhibit any distinct superlattice reflections, as could be expected for a fully coherent stacking of crystalline nano-layers.³⁷ This suggests that the structural coherence length along the growth direction is lower than the (measured) modulation period of ≈ 26 nm of the Ag-Cu/AlN building block. Indeed the average grain sizes (D) of $D_{\text{Ag}} \approx 6$ nm and $D_{\text{Cu}} \approx 4$ nm in the as-deposited NML (as obtained from the synchrotron analysis in Sec. 3.2) are smaller than the individual nano-layer thicknesses (≈ 15 nm and ≈ 11 nm for the alloy and the AlN barrier; see above).

The dominant reflections from Ag and AlN in Fig. 3b are all from Ag{111} and AlN{001} family of planes, which implies that the preferred growth directions of the Ag and the AlN nano-grains are parallel to Ag[111] and AlN[001], respectively. This finding is consistent with the most densely packed planes of Ag and AlN of lowest surface energy being parallel to the film surface.³⁸ Recorded XRD PHI-scans for AlN(103) and Ag(111) indicate that the AlN and the Ag nano-grains also exhibit in-plane texture obeying the epitaxial relationship $\text{Ag}\{111\}\langle 110\rangle\parallel\text{AlN}\{001\}\langle \bar{1}10\rangle$, in accordance with Ref.³⁹: see Fig. 4a. The

texture measurements (i.e. pole figures) of the Ag(002) and Cu(111) reflections show that the Cu nano-crystallites in the as-deposited NML exhibit the same, albeit a much less pronounced texture as compared to the Ag nano-grains (see Fig. 4b). Hence the phase-separated fcc Cu nano-grains are coherent with respect to the fcc matrix of Ag nano-grains. The observed six-fold symmetry in the measured Ag and Cu pole figures originates from the aforementioned epitaxial relationship between the AlN barrier and the Ag crystallites, because 60° in-plane rotated Ag{111} domains on the AlN{001} are equally preferred from an energetic point of view. A six-fold symmetry in the measured Ag and Cu pole figures could also partly originate from twinning of the Ag nano crystallites (also inducing twin orientations in coherent Cu grains), as commonly observed for metals with a relatively low stacking fault energy, like Ag.⁴⁰ Notably a columnar or fibre structure of the Ag and Cu crystallites, as frequently reported for sputter-deposited (nano-crystalline) single-alloyed fcc alloys was not evidenced in the present study (i.e. the average crystallite size in the present study is less than the layer thickness; see above).^{6,41}

The two broad and low intensity peaks at $2\theta = 42.67^\circ$ and $2\theta = 73.04^\circ$ in Fig. 3b are close to the Cu(111) and Cu(220) reflections of bulk Cu metal, respectively. However the detected Cu content in the Ag-Cu nano-layers (as estimated from intensity ratio of the detected Ag{111} and Cu{111} reflections, taken into account the fact that the Ag and Cu nano-grains have the same texture) is much less, as would be expected for a completely phase-separated bulk-eutectic Ag-Cu alloy constituted of pure Ag and pure Cu nano-grains. It is therefore concluded that the eutectic Ag-Cu nano-layers are constituted of Ag nano-grains ($D_{\text{Ag}} \approx 6$ nm), which are supersaturated by Cu, and a much lower content of Cu nano-grains ($D_{\text{Cu}} \approx 4$ nm). The confined Ag-Cu nano-layers thus do not comply with a homogenous (super) saturated nano-crystalline Cu-Ag solid solution phase, as reported in Refs.^{2,6,12}. In the present study, we consciously refrain from estimating the Cu content in the supersaturated Ag nano-grains, because the peak positions of the detected diffraction lines will not only depend on the composition of the nano-crystallites, but also on the nano-grain size and superimposed residual growth stresses.

A rocking curve (RC) scan of the Ag(111) reflection was measured to reveal the degree of in-plane coherency of the supersaturated Ag nano-crystallites in the as-deposited state: see Fig. 4d. RCs provide detailed information on the in-plane correlation function of textured grains and/or the angular distribution of randomly oriented crystal domains.⁴² The full-width-at-half-maximum (FWHM) of the measured Ag(111) RC directly relates to the in-

plane coherency length of [111]-oriented Ag domains. The measured RCs for both Ag and AlN have a Gaussian line shape with a FWHM of more than 5° , indicating an angular distribution of the corresponding domains of roughly 5° .⁴² Thus although the Ag-Cu/AlN NML exhibits a pronounced texture, a substantial degree of disorder due to mozaicity, in-plane roughness and defects originates from the sputter deposition process.

3.2. Microstructural evolution during heating up to 420°C

The 2 θ scans, as recorded in transmission at the synchrotron with a time resolution of about 40s during fast heating up to 420°C (Fig. 1), are plotted as a function of the temperature in Fig. 5a. The most pronounced Ag(222) and Cu(222) reflections from the confined nanoalloy grow in intensity and become narrower during heating, whereas the much weaker Ag(311) and Ag(511) reflections gradually disappear during heating. The evolutions of the FWHM of the Ag(222) and Cu(222) reflections upon heating are shown in Figs. 5b and 5c, respectively. Notably, the evolutions of the FWHMs of the Ag(222) and Cu(222) peaks during heating are remarkably different (see Fig. 5b). The FWHM of the Ag(222) peak remains constant in the range of 0.53 - 0.55 up to 265°C and then abruptly decreases to 0.50° in the T -range from 265°C to 350°C, reaching a FWHM of about 0.5° at 420 °C. The FWHM of the Cu(222) peak, on the other hand, gradually decreases from the onset of heating, first slowly up to 265°C and then more rapidly up to about 350 °C, attaining a much smaller FWHM of 0.12° at 420 °C (as compared to the final FWHM of about 0.5° for the Ag(222) peak). A rough estimation of the average Ag and Cu crystallite sizes (D) can be obtained from the FWHM values using the so-called Sherrer formula, $D = \frac{0.94 \lambda}{\beta \cos \theta}$, where λ is the photon wavelength, β is the FWHM (in radians) and θ is the corresponding Bragg angle.⁴³ It should be noted that this simple procedure gives an estimation of the average coherency length of the chosen family of planes, rather than a quantitative measure of the “real” grain size of the crystallites. Applying this procedure to the FWHMs in Fig. 5b, gives average grain sizes of $D_{\text{Ag}} = 6$ nm and $D_{\text{Cu}} = 4$ nm for α -Ag and β -Cu in the as-deposited NML, respectively (both smaller than the layer thickness of the confined alloy of ~ 15 nm; see Fig. 2a). Applying to the FWHMs after heating at 420 °C, results in estimated average grain sizes of $D_{\text{Ag}} = 7$ nm and $D_{\text{Cu}} = 26$ nm. This indicates that the Ag and Cu nano-grains undergo coarsening during heating. Notably the other reflections (not belonging to the {111} family of planes) become weaker during heating.

As evidenced by XRD, XPS and SEM analyses (see below and Sec. 3.3), protrusions of Cu metal have appeared at the NML surface after heating and annealing up to 420 °C. This suggests that the initially confined Cu nano-grains have (partially) relocated to the NML surface during heating, where they can coarsen at a much faster rate than the still confined nano-grains. Hence, the average Cu grain-size of 26 nm after heating, as estimated from the FWHM of the Cu(222) peak (see above), is governed by the signal contribution of the large (unstrained) Cu protrusions accumulated at the NML surface during heating. Indeed, the estimated Cu grain size of 26 nm is by far larger than the thickness of the Ag-Cu nano-layers.

Since the (linear) thermal expansion coefficients of Ag ($\alpha_{\text{Ag}} \approx 18 \times 10^{-6} \text{ K}^{-1}$) and Cu ($\alpha_{\text{Cu}} \approx 17 \times 10^{-6} \text{ K}^{-1}$) in the confined alloy nano-layers are much larger than that of the much thicker and rigid $\alpha\text{-Al}_2\text{O}_3$ substrate ($\alpha_{\text{sapphire}} \approx 8 \times 10^{-6} \text{ K}^{-1}$, close to that of $\alpha_{\text{AlN}} \approx 5 \times 10^{-6} \text{ K}^{-1}$), the ensemble of confined Ag and Cu crystallites in the alloy nano-layers becomes compressively strained upon heating. Outflow of Cu to the NML surface during heating would thus result in (partial) relaxation of the accumulated thermal stresses, in accordance with the observed abrupt decrease in the FWHM of the Ag(222) reflections at $T > 265^\circ\text{C}$ (see Fig. 5b). To qualitatively investigate the thermal stress evolution in the NML during heating, the Ag(222), Cu(222) and $\text{Al}_2\text{O}_3(223)$ lattice spacings and their (approximately linear) thermal expansion coefficients were deduced from the recorded diffractograms: see Figs. 6(a-c). Since the $\alpha\text{-Al}_2\text{O}_3$ substrate is infinitely thick and rigid as compared to the NML, the thermal expansion of the alloy and AlN nano-layers will be dictated by the thermal expansion of the sapphire substrate. Indeed, up to 350°C, the estimated average thermal expansion coefficient of the confined nano-alloy roughly lies in between $\alpha_{\text{Ag}} \approx 7.3^{\pm 0.1} \times 10^{-6} \text{ K}^{-1}$ and $\alpha_{\text{Cu}} \approx 11.6^{\pm 0.4} \times 10^{-6} \text{ K}^{-1}$, in accordance with the intermediate experimental value of $\alpha_{\text{sapphire}} \approx 8.1^{\pm 0.4} \times 10^{-6} \text{ K}^{-1}$ (see Fig. 6). Notably, beyond 350°C, the thermal expansion coefficient of Cu abruptly increases to $\alpha_{\text{Cu}} \approx 29.9^{\pm 0.2} \times 10^{-6} \text{ K}^{-1}$, while those of Ag and AlN still (roughly) comply with that of Al_2O_3 . This finding also relates well with the accumulation of Cu at the top of the NML at around 350°C, where it can (more) freely expand (since it is no longer confined).

Notably $\text{Cu}_2\text{O}(200)$ reflections appear at $T > 265^\circ\text{C}$, as attributed to (partial) oxidation of Cu metal, which has accumulated at the NML surface. Here it is noted that the in-situ heating experiment was carried out in Ar shielding gas (see Sec. 2.2), which cannot prevent a partial oxidation of Cu at the surface. As evidenced by post-mortem XPS depth profiling, remaining Cu grains inside the NML were not affected by oxidation during heating (see Sec.

3.3). This suggests that the outflow of Cu to the NML surface might also be partially driven by O-enhanced segregation of Cu to the NML surface. The recorded diffractograms do not show any more significant changes for $T > 400$ °C, as well as upon subsequent isothermal annealing at $T = 420$ °C. The in-situ real-time XRD study evidences that phase separation and grain coarsening during heating runs parallel with the outflow and accumulation of Cu at the NML surface, leading to a partial relaxation of compressive thermal stresses in the confined nano-alloy layers.

3.3. NML microstructure after heat treatment

SEM micrographs of the heat-treated NML in planar and cross-sectional view are shown in Figs. 7a and b, respectively. Table 1 gives the average chemical composition of the as-deposited and heat-treated NML, as obtained from averaging a series of EDX point measurements recorded from the top surface. After fast heating to 420 °C, a high density of line-shaped features and spherical-shaped protrusions appeared on the NML surface (as indicated by white and black arrows in Fig. 7a, respectively). The original as-deposited NML surface was very smooth (see Fig. 2) and thus no distinct correlations between the occurrence of lines features and/or spherical protrusions at the heat-treated NML surface and apparent growth defects in the as-deposited state could be identified. The EDX analysis shows that the average composition of the NML is largely unaffected by the heat treatment up to 420 °C (Table 1). In order to probe the chemical composition of the spherical protrusions on the heat-treated NML surface, EDX point-measurements of big protrusions (diameter $> 2\mu\text{m}$) were performed, which revealed that they mainly consist of Cu and O (in agreement with the XRD analysis).

The cross-sectional SEM micrograph was taken roughly perpendicular to an observed line shaped feature: see Fig. 7b. Phase contrast variations could be observed within the alloy nano-layer (corresponding to the bright layers in Fig. 7b), confirming that large domains of phase-separated Ag and Cu developed after heating up to 420 °C. At first view, the layer configuration directly underneath the Cu surface protrusion in the cross-sectional electron micrograph of Fig. 7b seems to be more or less intact. However, closer investigation evidences that the top AlN and Ag-Cu surface layers seem to be partially missing, as indicated by black dashed lines in Fig. 7b.

The measured XPS composition-depth profile of the heat-treated NML is shown in Fig. 8. Please note that the surface coverage of (oxidized) Cu protrusions at the heat-treated

NML surface is statistically too low to significantly contribute to the XPS depth-profiling analysis.¹ The XPS analysis of the heat-treated NML clearly indicates that Cu is depleted from the top three alloy layers adjacent to the surface. Notably, the first surface-adjacent layer is practically fully depleted of Cu (with the remaining Cu being oxidized). Also deeper inside the NML (i.e. after the first three AlN/Ag-Cu units from the top), the Cu concentration still appears lower as compared to the as-deposited state (although the XPS quantification of the annealed NML is rather critical²). Furthermore, the XPS analysis indicates that a reaction between Cu and AlN (forming e.g. Cu-nitride compound) has not occurred.

Except for the rupture and local disappearance of the first surface-adjacent barrier and alloy nanolayers, the outflow of Cu during heating up to 420 °C has not resulted in significant morphological changes within the NML structure. Noteworthy, significant morphological changes due to layer collapse and sintering of AlN barriers have recently been observed for annealing of Cu/AlN NML coating systems at more elevated temperatures of 750 °C.⁴⁷

X-ray diffractograms of the Ag-Cu/AlN NML before and after heat treatment up to 420°C are shown in Fig. 9 (as recorded in Bragg-Brentano and grazing incidence geometry). The grazing incidence analysis in Fig. 9b clearly evidences the enrichment of (partially oxidized) Cu at the NML surface after the heat treatment, in accordance with the accumulation of Cu at the NML surface after heating (see Sec. 3.2). The measured pole figures and RCs of the NML before and after heating are presented in Fig. 4 (see Sec. 3.1). The pole figures of the annealed NML appear much more blurred due to the fact that the intensity maxima are submerged into a very high background (which is much higher than for the as-deposited NML). The very high background signal in the pole figures of the heat-treated NMLs most probably originates from a random in-plane texture of the accumulated Cu protrusions on the NML surface (introducing a high background signal to the measured pole figures). Nevertheless, the increased sharpening of the intensity maxima from Ag and Cu in the pole figure of Fig. 4b, as well as the much narrower RC curve in Fig. 4d, evidence that the

¹ A single Cu protrusion of $1 \times 1 \mu\text{m}^2$ only contributes about 0.01% to the XPS analysis of $100 \times 100 \mu\text{m}^2$, which is well below the XPS detection limit.

² Please note that the XPS sputter-depth profile of the heat-treated NML was not corrected for preferential sputtering of Ag. Consequently, the measured *steady-state* Cu concentration in the eutectic alloy, as reached during sputter-depth profiling, should approach 60 at.% (see Sec. 2.2), which is not observed in the concentration-depth profile of Fig. 8. This implies that Cu also may have depleted to some extent from deeper inside the NML after heat-treatment up to 420 °C.

confined Ag (and remaining Cu) crystallites have not only increased in size upon heating, but also increased their in-plane coherency with respect to the AlN barrier. Moreover, a shift of the Ag(111) lattice spacing towards the bulk value of 2.359 Å has occurred, as attributed to the combined effect of stress relaxation and segregation of Cu out of the initially (super)saturated α -Ag grains.

4. Chemical driving forces for structural transformation

As evidenced in Sec. 3, the as-deposited Ag-Cu /AlN NML is constituted of a regular stacking of alternating nano-layers of a eutectic Ag-Cu alloy and an AlN barrier (with individual thicknesses in the range of 10 to 15 nm). The individual Ag-Cu nano-layers are composed of a fcc matrix of Ag nano-grains ($D_{\text{Ag}} \approx 6$ nm), which are supersaturated by Cu, and some smaller embedded Cu rich nano-grains ($D_{\text{Cu}} \approx 4$ nm). Hence phase segregation on the nano-scale has already occurred during sputter deposition at RT (i.e. a homogeneous solid-solution phase has not formed), as driven by high positive enthalpy of mixing (see Sec. 1). The texture of the confined Ag and Cu nano-grains is dictated by the AlN barrier and follows the orientation relationships: $\text{Ag}\{111\}\langle 110\rangle\|\text{AlN}\{001\}\langle \bar{1}10\rangle$ and $\text{Cu}\{111\}\langle 110\rangle\|\text{AlN}\{001\}\langle \bar{1}10\rangle$.

Heating of the NML up to 265 °C induces segregation of Cu out of the supersaturated Ag nano-grains. At $T > 265$ °C, Cu migrates out of the surface-adjacent alloy nano-layers to the top of the NML surface, thereby partially relaxing thermally-accumulated compressive stresses in the confined alloy nano-layers and facilitating (i.e. accelerating) grain coarsening of (still confined) phase-separated nano-crystallites. The Gibbs energy of incoherent (i.e. high-energy) grain-boundary metals is roughly proportional to one third of the surface energy of the metal.⁴⁶ The surface energies of Cu and Ag metal equal 1.79 J/m² and 1.25 J/m², respectively,¹⁹ which suggests that (high-angle) grain boundaries between neighbouring Cu nano-grains are higher in energy than neighbouring Ag nano-grains. Hence confined Cu nano-crystallites possess a higher driving force for grain coarsening (to reduce the total grain boundary energy) than Ag nano-grains.

The subsequent *abrupt* outflow of Cu to the NML surface at around 265°C could hint at a thermally-activated wetting transition of AlN grain-boundaries (or triple junctions) by Cu with concurrent fast diffusion of compressed Cu through the wetted “channels”.⁴⁴ The Ag/AlN interfaces become more coherent during heating, in accordance with recent DFT calculations of the atomic structure of the (relaxed) Ag/AlN interface (see Fig. 10a).³⁹ The

coherent Ag/AlN interface associated with phase-separated Ag domains is preferred with respect to the relaxed semi-coherent Cu/AlN interface (associated with phase-separated Cu nano-grains). As illustrated by the DFT structures of the Ag/AlN and Cu/AlN interfaces in Fig. 10b (adopted from Ref. ³⁹), the semi-coherent Cu/AlN interface contains a higher density of lattice misfit dislocations and/or point defects. As a result, the atomic mobility of Cu along the semi-coherent Cu/AlN interface will be considerably higher (as compared to the atomic mobility of Ag along the Ag/AlN interface), thereby facilitating transport of Cu along internal Cu/AlN interfaces to defective sites (i.e. permeable channels) in the AlN barrier layers for outward migration of Cu to the NML surface (comparable to the diffusion and subsequent wetting of Al grain boundaries by Si at strikingly low temperatures of 200 °C; cf. Ref. ⁴⁶). As evidenced from the partial oxidation of the outflowing Cu, the outward migration of compressed Cu might also be partially driven by O-induced surface segregation.

The concurrent processes of Cu segregation out of (super)saturated Ag grains, grain coarsening (reduction of the grain boundary density), slight in-plane grain rotations of phase-separated Ag and Cu crystallites (increasing in-plane coherency) and thermal stress relaxation, all contribute to a lowering of the Gibbs energy of the system. The abrupt and fast outflow of confined Cu from the Ag-Cu nano-layers at strikingly low temperatures might open new routes for joining at temperatures well below the melting temperature of the eutectic Ag-Cu alloy. It still remains to be clarified if the observed very fast kinetics of this process is accompanied by (partial) interfacial melting of Cu at the semi-coherent Cu/AlN interface and/or a grain-boundary-wetting phase transition in the AlN barrier layers (i.e. instantaneous wetting of AlN grain boundaries by Cu at around 265°C).

Conclusions

A bulk-eutectic AgCu_{40at.%} nano-alloy, as confined between AlN barrier, was prepared by magnetron sputtering at room temperature. The confined nano-alloy is composed of a fcc matrix of Ag nano-grains (≈ 6 nm), which are supersaturated by Cu, and some smaller embedded Cu rich nano-grains (≈ 4 nm). The texture of the confined Ag and Cu nano-grains is dictated by the AlN barrier, following the orientation relationships Ag{111}<110>||AlN{001}<-110> and Cu{111}<110>||AlN{001}<-110>. The Cu nano-crystallites exhibit a less pronounced texture than the supersaturated Ag nano-grains.

Heating up to 265°C induces segregation of Cu out of the supersaturated Ag nano-grains. At $T > 265$ °C, Cu migrates out of the surface-adjacent alloy nano-layers to the top NML surface, thereby partially relaxing thermally-accumulated compressive stresses in the

confined alloy nano-layers. Evidently, migration of Cu from the interior towards the NML surface is observed at temperatures well below the bulk melting temperature of Cu. Relaxation of thermal stresses by outflow of Cu facilitates (i.e. accelerates) grain coarsening of (still confined) phase-separated nano-crystallites within the multilayer, leading to an increased coherency of, in particular, the Ag/AlN interface. Further heating and annealing up to 420°C results in complete phase separation, forming extended confined Ag and Cu domains.

The structural evolution of the Ag-Cu/AlN NML coating upon heating is driven by a large positive enthalpy of mixing (inducing Cu segregation out of (super)saturated Ag grains), relaxation of accumulated thermal stresses (promoting outflow of Cu metal), reduction of the grain boundary density (by grain coarsening of Ag and Cu nano-crystallites) and reduction of interface energies (by slight in-plane grain rotations of phase-separated Ag and Cu crystallites).

The observed outflow of Cu at temperatures well below the melting point of the eutectic Ag-Cu alloy offers opportunities for the development of new nanostructured joining materials for joining at ever-lower temperatures, as demonstrated for similar Cu/AlN NML coating systems in Ref. ⁴⁷.

Acknowledgements

Support is acknowledged from COST Action MP0903 “Nanoalloys as advanced materials: from structure to properties and applications”. We acknowledge the Paul Scherrer Institut, Villigen, Switzerland for provision of synchrotron radiation beamtime at beamline X03MA of the SLS and would like to thank N. Casati for assistance. We acknowledge Prof. George Kaptay, Dr. Daniel Ariosa, Dr. Jörg Patscheider, Dr. Andrej Antusek, Dr. Daniele Passerone, Dr. Carlo Pignedoli and Prof. Riccardo Ferrando for fruitful discussions on the subject. Furthermore we acknowledge the access to the sputtering facilities and IPAZIA cluster at Empa.

References

1. E.Ma, *Progress in Mater. Science*, 2005, **50**, 413.
2. H.W. Sheng, G. Wilde and E. Ma, *Acta Mater.*, 2002, **50**, 475.
3. B. Y. Tsaur, S. S. Lau and J. W. Mayer, *Appl. Phys. Lett.*, 1980, **36**, 823.
4. K. Uenishi, K.F Kobayashi, K.N. Ishihara and P.H. Shingu, *J. Mater. Sci. Eng. A*, 1991, **134**, 1342.
5. R. Najafabadi, D.J.Srolovitz, E.Ma and M. Atzmon, *J. Appl. Phys.*, 1993, **74**, 3145.
6. F. Misják, P.B Barna and G Radnóczy, *Thin Solid Films*, 2010, **518**, 4247.
7. R. Asthana, M. Singh, *J. Eur. Ceram. Soc.*, 2008, **3**, 617.
8. J.H.Xiong, J.H.Huang, H. Zhang and X.K.Zhao, *J.Mater. Sci. Eng. A*, 2010, **527**, 1096.
9. Y.Li, P.He and J.Feng, *Scr. Mater.*, 2006, **55**, 171.
10. E. Lugscheider and W. Tillmann, *Mater. Manuf. Processes*, 1993, **8**, 219.
11. V. Bissig, M. Galli and J. Janczak-Rusch, *Adv. Eng. Mater.*, 2006, **8**, 191.
12. D. I. Filoti, A. R. Bedell and J. M. E. Harper, *J. Vac. Sci. Technol. A*, 2010, **28**, 838.
13. S. Gohil, R. Banerjee, S.Bose and P. Ayyub, *Scripta Materialia*, 2008, **58**, 842.
14. A.G. Dirks, J.J. van den Broek and P.E. Wierenga, *J. Appl. Phys.*, 1984, **55**, 4248.
15. P.B. Barna, M. Adamik, J. Lábár, L. Köver, J. Tóth, A. Dévényi and R. Manaila, *Surf. Coat. Technol.*, 2000, **125**,147.
16. H. Chen and J M Zuo, *Acta Mater.*, 2007, **55**, 1617.
17. J. H. He, H. W. Sheng, J. S. Lin, P. J. Schilling, R. C. Tittsworth, and E. Ma, *Phys. Rev. Lett.*, 2002, **89**, 125507
18. C. N. J. Wagner, T. B. Light, N. C. Halder and W. E. Lukens, *J. Appl. Phys.*, 1968, **39**, 3690.
19. L. Vitos, A.V. Ruban, H.L. Skriver and J. Kollár, *Surf. Sci.*, 1998, **411**, 186.
20. J. Y Wang, J du Plessis, J. J Terblans, G. N van Wyk, *Surf. Sci.*, 1999, **423**,12.
21. Q.S. Mei, K. Lu, *Progress in Mater. Sci.*, 2007, **52**, 1175.
22. G. Kaptay, J. Janczak-Rusch, G. Pigozzi, and L.P.H. Jeurgens, *J. Mater. Eng. Proc.*, 2014, **23**,1600.
23. G.Garzel, J. Janczak-Rusch and L.Zabdyr, *Calphad*, 2012, **36**, 52.
24. S. Li, W.Qi, H.Peng, J.Wu, *Comput. Mater. Sci.*, 2015, **99**, 125.
25. C. Langlois, Z. Y. Li, J. Yuan, D. Alloyeau, J. Nelayah, D. Bochicchio, R. Ferrando and C. Ricolleau, *Nanoscale*, 2012, **4**, 3381.
26. D. Bochicchio and R. Ferrando, *Eur. Phys. J. D*, 2012; **66**, 115.

27. J. Zhong, L.H. Zhang, Z.H. Jin, K. Lu K. *Acta Mater.*, 2001,**49**, 2897.
28. H. W. Sheng, *Philos. Mag. Lett.*, 1996, **73**, 176.
29. R.W. Cahn, *Nature*, 1986, **323**, 668.
30. K. Lu K, Z.H. Jin, *Curr. Opin. Solid State Mater. Sci.*, 2001,**5**,39.
31. K.S. Tan, K.Y. Cheong, *Mater. Design*, 2014, **64**, 166.
32. J. Janczak-Rusch, G. Kaptay and L.P.H. Jeurgens, *J. Mater. Eng. Proc.*, 2014, **23**, 1608.
33. J. Janczak-Rusch, G. Pigozzi, B. Lehmert, M. Parlinska, V. Bissig, W. Tillmann, L. Wojarski, F. Hoffmann: Proc. of IBSC 2012 - 5th International Brazing and Soldering Conference, 2012, 163.
34. P.R. Willmott et al., *J. Synchrotron Rad.* 2013, **20**, 667.
35. A. Bergamaschi et al., *J. Synchrotron Rad.* 2010, **17**, 653.
36. Y.Okajima, *J. Appl. Phys.*, 1980, **51**, 715.
37. E. E. Fullerton, I. K. Schuller, H. Vanderstraeten, and Y. Bruynseraede, *Phys. Rev. B*,1992, **45**, 9292.
38. F. Reichel, L.P.H. Jeurgens, E.J. Mittemeijer, *Acta Mater.*, 2008, **56**, 659.
39. G. Pigozzi, A. Antusek, J. Janczak-Rusch, M. Parlinska-Wojtan, D. Passerone, C.A. Pignedoli, V. Bissig, J. Patscheider and L.P.H. Jeurgens, *Appl. Phys.Lett.*, 2012, **101**, 181602.
40. N.A. Mara, I.J. Beyerlein, J. S. Carpenter, J. Wang, *J. Mater.*, 2012, **64**, 1218.
41. S. Nag, K. C. Mahdak, A. Devaraj, S.Gohil, P. Ayyub and R. Banerjee, *J.Mater. Sci.*, 2009, **44**, 3393.
42. A. Guinier in X-ray Diffraction in Crystals, Imperfect Crystals, and Amorphous Bodies, Courier Corporation, 1994.
43. A. Patterson, *Phys. Rev.*, 1939, **56**, 978.
44. C. Cai and J. K. Lumpp, *J. Mater. Res.*, 2001, **16**, 670.
45. Z. Wang, L. Gu, L.P. H. Jeurgens, F. Phillipp, and E. J. Mittemeijer, *Nano Lett.*, 2012, **12**, 6126.
46. L.P.H. Jeurgens, Z.M. Wang, E.J. Mittemeijer, *Intern. J. Mater. Res.*, 2009, **100**, 1281.
47. B. Lehmert, J. Janczak-Rusch, G. Pigozzi, P. Zuraw, F. La Mattina, L. Wojarski, W. Tillmann, L.P.H. Jeurgens, *Mater. Trans.*, 2015, accepted.

List of Figures

Fig. 1: Temperature-time program during in-situ heating and simultaneous XRD analysis of the as-deposited Ag-Cu/AlN NMLs.

Fig. 2: (a) Cross-sectional secondary electron image (light grey: Ag-Cu, dark grey: AlN) and (b) composition-depth profile measured by XPS, of the as-deposited Ag-Cu/AlN NML. The insert in (a) shows a SEM micrograph of the NML surface.

Fig. 3: X-ray diffractograms, as recorded from the as-deposited Ag-Cu/AlN NMLs at room temperature, (a) in transmission geometry at the synchrotron and (b) in Bragg-Brentano geometry in the laboratory. See Sec. 2.2 for details.

Fig. 4: (a) PHI scans of AlN(103) and Ag(111) reflections, as recorded from the as-deposited NML. (b) Pole figure of the Ag(200) and Cu(111) reflections, as recorded from (b) the as-deposited and (c) the thermally-treated NML. (d) Rocking curve around the Ag(111) reflection, as recorded from the as-deposited and thermally-treated NML.

Fig. 5: (a) Measured 2θ diffractograms as a function of temperature (in the range from RT to 420 °C), as recorded from the Ag-Cu/AlN NML in transmission at the synchrotron with a time resolution of about 40 s during fast heating up to 420 °C (following the temperature program pertaining to Fig. 1). The corresponding evolutions of the FWHM of the Ag(222) and Cu(222) peaks are plotted in (b) and (c), respectively.

Fig.6: (a) Cu(222), (b) Ag(222) and (c) Al₂O₃(223) lattice spacings as a function of temperature (in the range from RT to 420°C), as extracted from the corresponding diffractograms recorded from the Ag-Cu/AlN NML in transmission at the synchrotron with a time resolution of about 40s during fast heating up to 420°C (see Fig. 1). The respective linear thermal expansion coefficients (as deduced by linear least squares fitting) are also reported.

Fig. 7: Secondary electron micrographs of the heat-treated Ag-Cu/AlN NML in (a) planar view and (b) cross-sectional view. Lines and spherical features, which are present on the NML surface, are indicated by black and white arrows in (a), respectively. Phase contrast is resolved inside the heat-treated Ag-Cu layers in (b) (light grey: Ag-Cu, dark grey: AlN).

Fig. 8: Composition-depth profile measured by XPS, of the Ag-Cu/AlN NML after heat treatment up to 420 °C.

Fig. 9: Measured X-ray diffractograms, as recorded from the Ag-Cu/AlN NMLs before (as-deposited) and after heat treatment up to 420 °C; (a) θ - 2θ scan in Bragg-Brentano geometry and (b) grazing incidence diffraction scan at fixed $\omega = 5^\circ$. The peaks indicated with an asterisk () are parasitic peaks due to the not-fully monochromatic radiation.*

List of Tables

Table 1: EDX point measurements of the AgCu/AlN NMLs in the as-deposited state and after fast heating to 420 °C. The average value and error in the concentration was obtained from averaging a series of five EDX point.

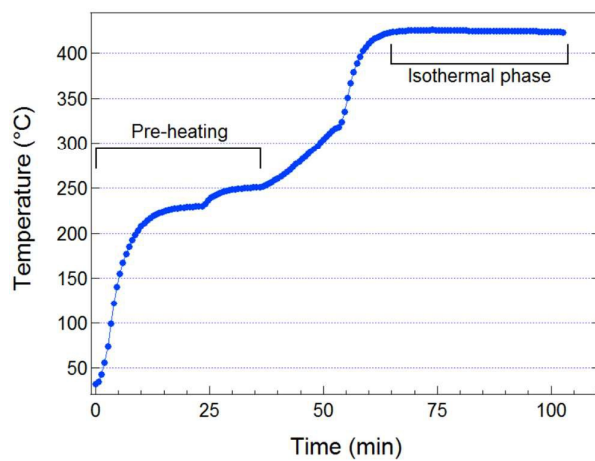


Fig. 1: Temperature-time program during in-situ heating and simultaneous XRD analysis of the as-deposited Ag-Cu/AlN NMLs.

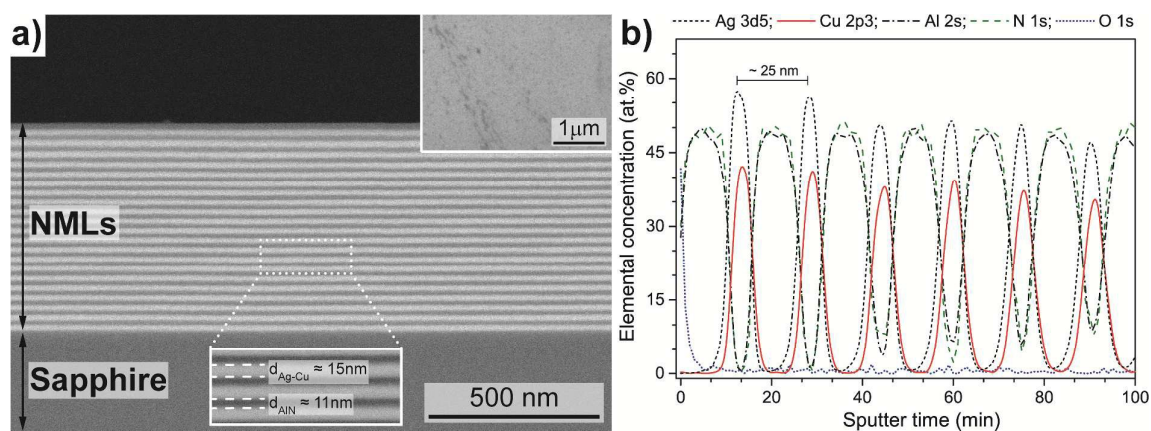


Fig. 2: (a) Cross-sectional secondary electron image (light grey: Ag-Cu, dark grey: AlN) and (b) composition-depth profile measured by XPS, of the as-deposited Ag-Cu/AlN NML. The insert in (a) shows a SEM micrograph of the NML surface.

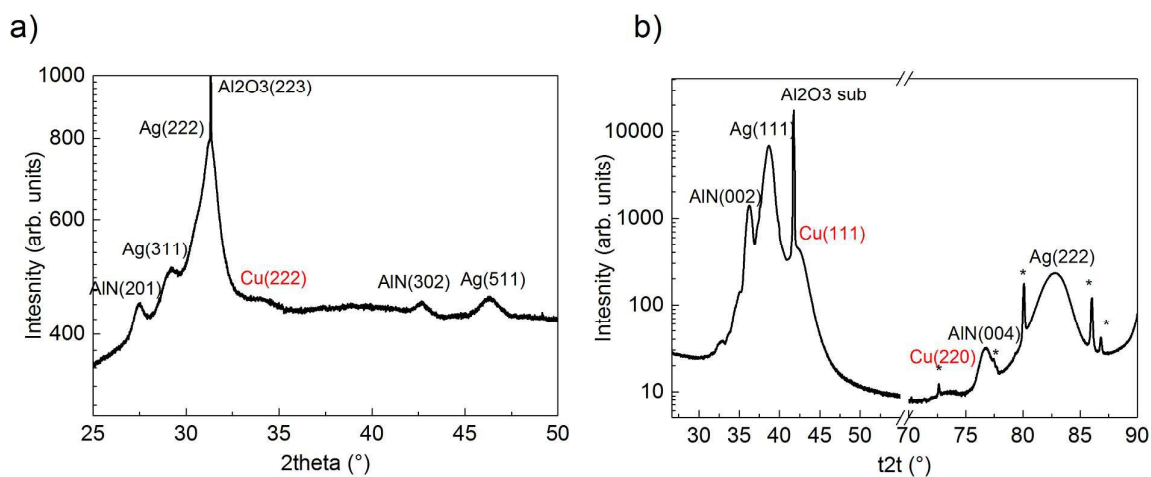


Fig. 3: X-ray diffractograms, as recorded from the as-deposited Ag-Cu/AlN NMLs at room temperature, (a) in transmission geometry at the synchrotron and (b) in Bragg-Brentano geometry in the laboratory. See Sec. 2.2 for details.

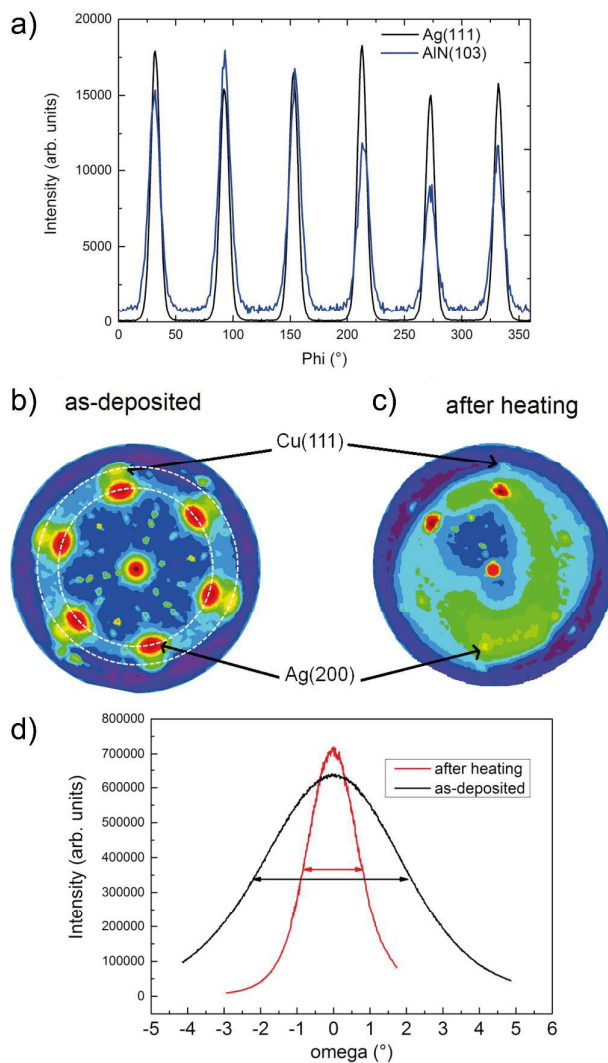


Fig. 4 (a) PHI scans of AlN(103) and Ag(111) reflections, as recorded from the as-deposited NML. (b) Pole figure of the Ag(200) and Cu(111) reflections, as recorded from (b) the as-deposited and (c) the thermally-treated NML. (d) Rocking curve around the Ag(111) reflection, as recorded from the as-deposited and thermally-treated NML

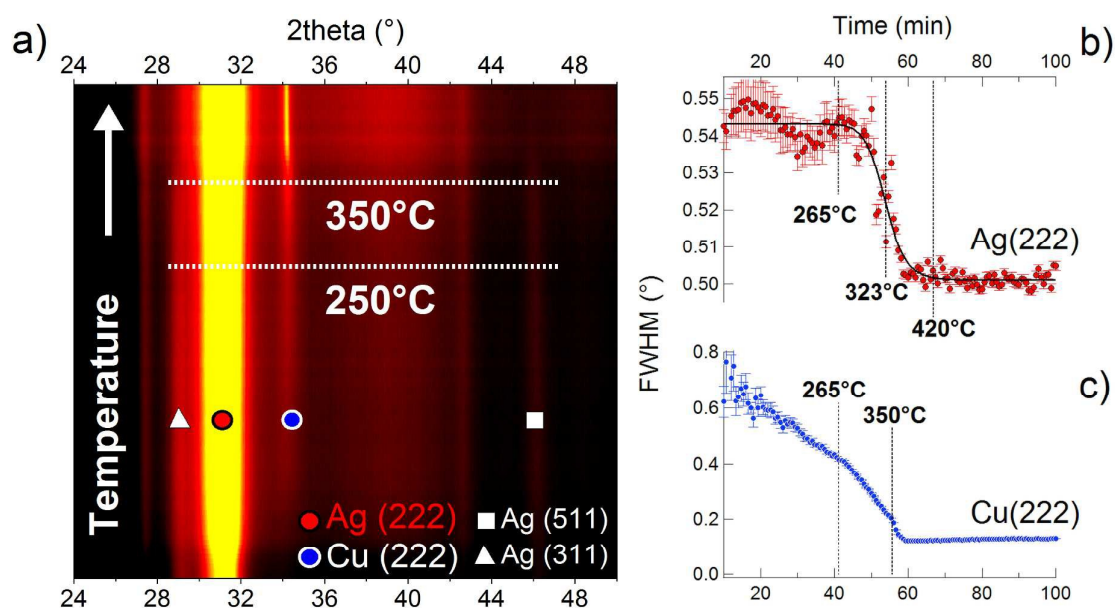


Fig. 5: (a) Measured 2theta diffractograms as a function of temperature (in the range from RT to 420 °C), as recorded from the Ag-Cu/AlN NML in transmission at the synchrotron with a time resolution of about 40 s during fast heating up to 420 °C (following the temperature program pertaining to Fig. 1). The corresponding evolutions of the FWHM of the Ag(222) and Cu(222) peaks are plotted in (b) and (c), respectively.

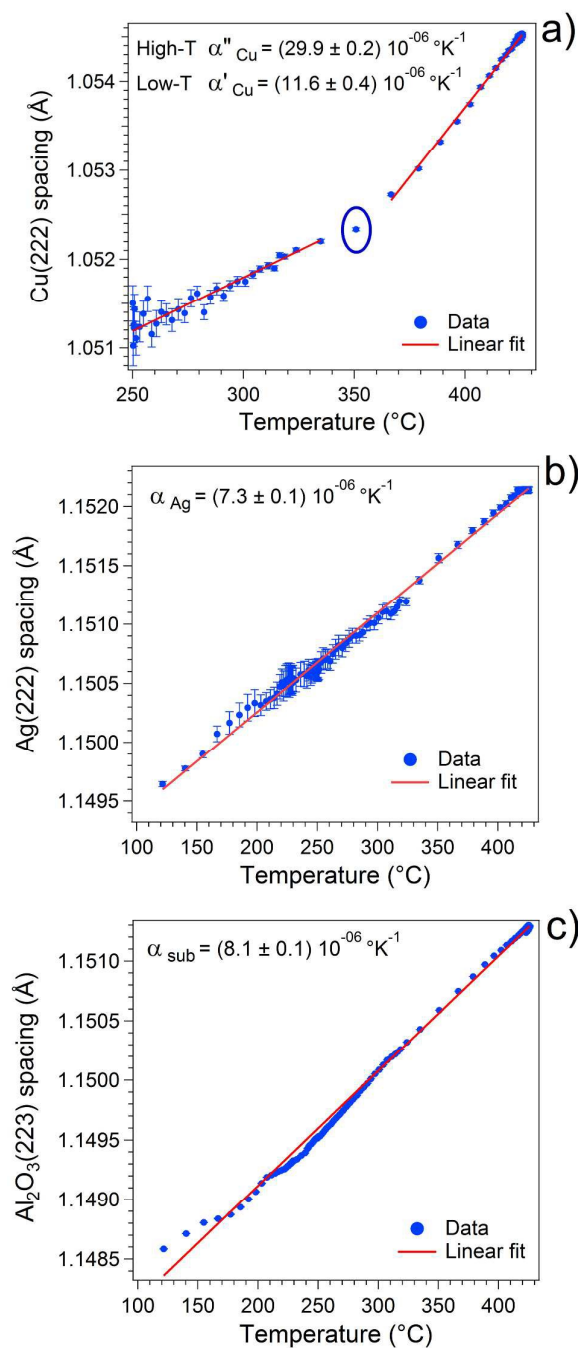


Fig.6: (a) Cu(222), (b) Ag(222) and (c) Al₂O₃(223) lattice spacings as a function of temperature (in the range from RT to 420°C), as extracted from the corresponding diffractograms recorded from the Ag-Cu/AlN NML in transmission at the synchrotron with a time resolution of about 40s during fast heating up to 420°C (see Fig. 1). The respective linear thermal expansion coefficients (as deduced by linear least squares fitting) are also reported.

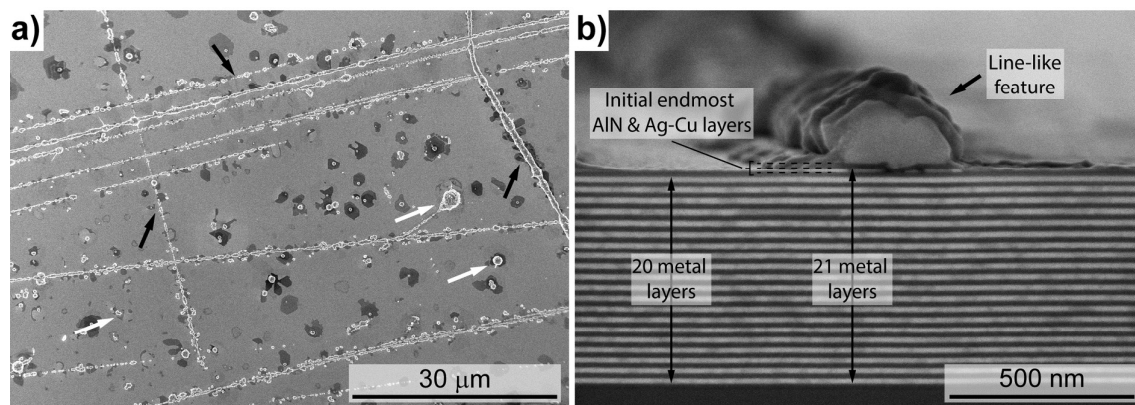


Fig. 7: Secondary electron micrographs of the heat-treated Ag-Cu/AlN NML in (a) planar view and (b) cross-sectional view. Lines and spherical features, which are present on the NML surface, are indicated by black and white arrows in (a), respectively. Phase contrast is resolved inside the heat-treated Ag-Cu layers in (b) (light grey: Ag-Cu, dark grey: AlN).

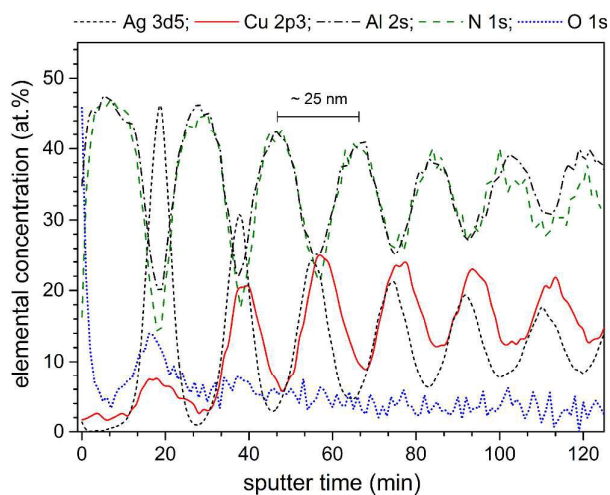


Fig. 8: Composition-depth profile measured by XPS, of the Ag-Cu/AlN NML after heat treatment up to 420 °C.

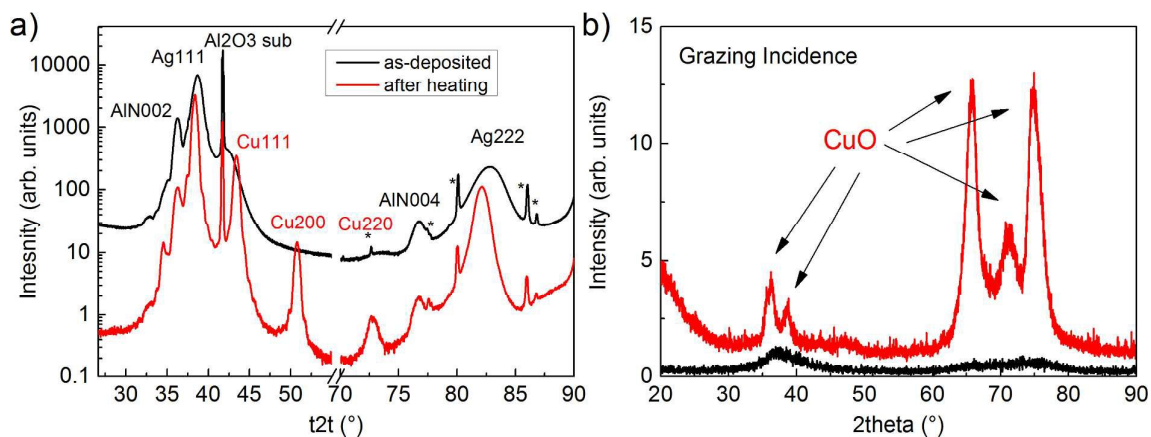


Fig. 9: Measured X-ray diffractograms, as recorded from the Ag-Cu/AlN NMLs before (as-deposited) and after heat treatment up to 420 °C; (a) θ - 2θ scan in Bragg-Brentano geometry and (b) grazing incidence diffraction scan at fixed $\omega = 5^\circ$. The peaks indicated with an asterisk (*) are parasitic peaks due to the not-fully monochromatic radiation.

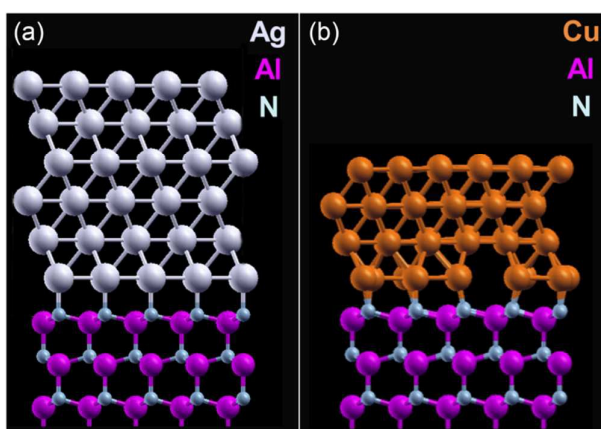


Fig. 10: Atomic structure of the (relaxed) (a) coherent Ag/AlN interface and (b) semi-coherent Cu/AlN interface (in cross-sectional view), as predicted by Density Functional Theory, DFT. Calculations were performed for different (relaxed) Ag and Cu slabs on the nitrogen-terminated $5 \times 5 \times 3$ AlN(000 $\bar{1}$) slab. See Ref. ³⁹ for details.

Table 1. EDX point measurements of the AgCu/AlN NMLs in the as-deposited state and after fast heating to 420 °C. The average value and error in the concentration was obtained from averaging a series of five EDX point.

As-deposited NML					
	Ag (at.%)	Cu (at.%)	Al (at.%)	N (at.%)	O (at.%)
Bare NMLs	19.0±0.3	12.4±0.5	32.9±2.4	34.3±4.0	1.4±0.8
Heat-treated NML (after fast heating to 420 °C)					
Bare NMLs	20.3±0.3	10.8±0.4	33.0±2.3	35.2±4.1	0.8±0.7
Cu protrusions	0.7±0.1	48.7±1.1	2.3±0.3	3.0±2.4	45.4±3.7